

EchoScan: Scanning Complex Indoor Geometries via Acoustic Echoes

Inmo Yeon, *Student Member, IEEE*, Iljoo Jeong, Seungchul Lee, and Jung-Woo Choi, *Member, IEEE*

Abstract—Accurate estimation of indoor space geometries is vital for constructing precise digital twins, whose broad industrial applications include navigation in unfamiliar environments and efficient evacuation planning, particularly in low-light conditions. This study introduces EchoScan, a deep neural network model that utilizes acoustic echoes to perform room geometry inference. Conventional sound-based techniques rely on estimating geometry-related room parameters such as wall position and room size, thereby limiting the diversity of inferable room geometries. Contrarily, EchoScan overcomes this limitation by directly inferring room floorplans and heights, thereby enabling it to handle rooms with arbitrary shapes, including curved walls. The key innovation of EchoScan is its ability to analyze the complex relationship between low- and high-order reflections in room impulse responses (RIRs) using a multi-aggregation module. The analysis of high-order reflections also enables it to infer complex room shapes when echoes are unobservable from the position of an audio device. Herein, EchoScan was trained and evaluated using RIRs synthesized from complex environments, including the Manhattan and Atlanta layouts, employing a practical audio device configuration compatible with commercial, off-the-shelf devices. Compared with vision-based methods, EchoScan demonstrated outstanding geometry estimation performance in rooms with various shapes.

Index Terms—Deep neural network, digital twin, room geometry inference, room impulse response

I. INTRODUCTION

DIGITAL twins have expedited innovative industrial applications spanning diverse sectors, such as navigating unfamiliar terrains or planning efficient evacuation blueprints [1]. The estimation of the indoor geometries is a crucial step in

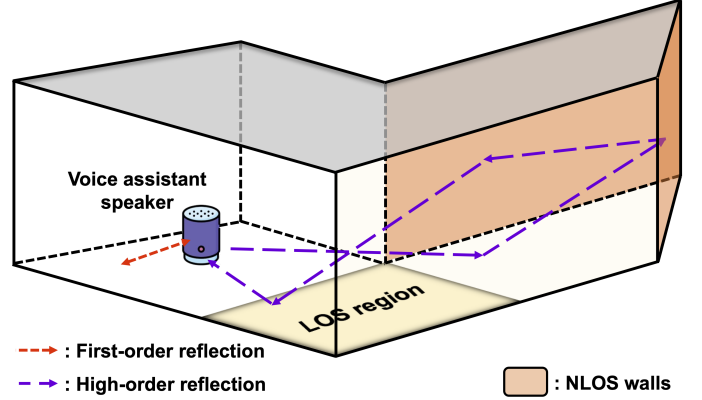


Fig. 1. Conceptual illustration of the indoor-geometry-estimation task using an audio device positioned in the NLOS region.

constructing realistic digital twins of indoor spaces. The methods for identifying indoor geometries have been studied using vision-based techniques. However, achieving accurate digital representations is challenging, particularly when visual data are limited or inaccessible. Cases with insufficient visual cues, such as disaster sites or power outages, highlight the inherent limitations of vision-based approaches. Even with visible light, the estimation of occluded geometries is fundamentally challenging for vision-based digital twin construction. For such situations, acoustic indoor geometry estimation has emerged as a promising alternative that demonstrates the advantages of acoustic wave propagation through complex structures.

Acoustic echoes encapsulate essential information on indoor geometrical characteristics [2]. When the sound emitted from an audio device interacts with room boundaries, interactions such as specular and diffuse reflection, diffraction, and scattering are captured as room impulse responses (RIRs). The representative features of RIRs for indoor geometry estimation are the time-of-arrival (TOA), which represents the duration required for sound to travel from a source to a receiver, and the direction-of-arrival (DOA), which indicates the impinging direction of the reflected waves.

For room geometry inference (RGI), researchers have notably focused on the TOAs of first-order reflections, which provide accurate distances to walls [3]–[12]. For instance, ellipses can be formed employing the collected TOAs of first-order reflections [3], [4] such that the two focal points of an ellipse correspond to the positions of a sound source and microphone. The boundary of the room can then be represented by a common tangential line across multiple ellipses. Remaggi *et al.* [9] compared several reflector localization

Manuscript received February 23, 2024

This study was supported by the National Research Council of Science and Technology (NST) funded by the Ministry of Science and ICT (MSIT) of Korea (Grant No. CRC 21011), the National Research Foundation of Korea (NRF) grant funded by the MSIT of Korea (Grant No. 1711091575), the BK21 FOUR program through the NRF funded by the Ministry of Education of Korea, the Institute of Civil-Military Technology Cooperation funded by the Defense Acquisition Program Administration and Ministry of Trade, Industry and Energy (MOTIE) of the Korean government (Grant No. 19-CM-GU-01), and the Korea Institute of Energy Technology Evaluation and Planning (KETEP) grant funded by the MOTIE of the Korean government (Grant No. 20206610100290).

(Inmo Yeon and Iljoo Jeong equally contributed to this work.) (Corresponding authors: Seungchul Lee; Jung-Woo Choi.)

Inmo Yeon and Jung-Woo Choi are with the School of Electrical Engineering, Korea Advanced Institute of Science and Technology (KAIST), Daejeon, 34141, South Korea. (e-mail: iyeon@kaist.ac.kr; jwoo@kaist.ac.kr)

Seungchul Lee is with the Department of Mechanical Engineering, Korea Advanced Institute of Science and Technology (KAIST), Daejeon, 34141, South Korea. (e-mail: seunglee@kaist.ac.kr)

Iljoo Jeong is with the Department of Mechanical Engineering, Pohang University of Science and Technology (POSTECH), Pohang, 37673, South Korea. (e-mail: iljjeong@postech.ac.kr)

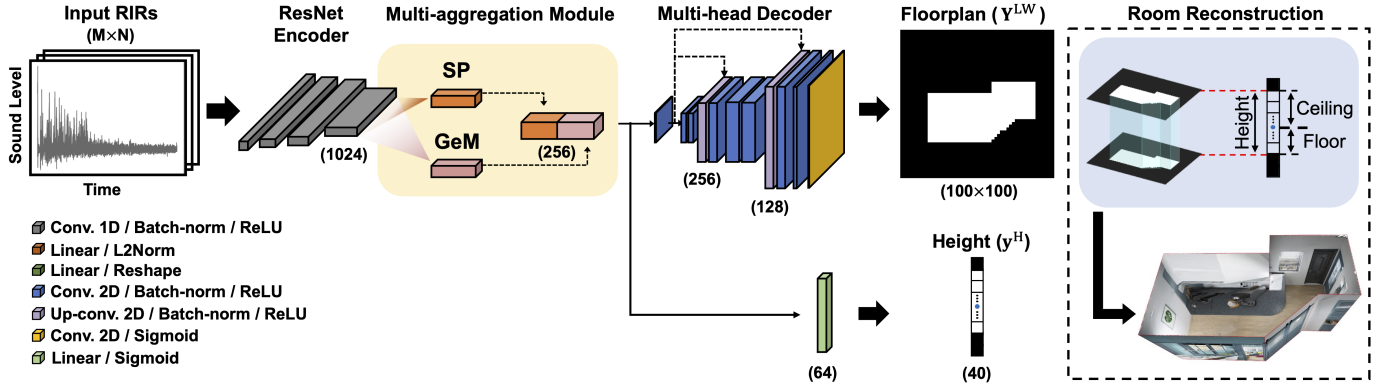


Fig. 2. Encoder-decoder architecture of the proposed EchoScan. The encoder extracts and aggregates spatial features using the MA module. The decoder generates two segmented images for the floorplan and height using its dual-head structure. The 3D geometry is then reconstructed by extruding the floorplan image in height.

techniques and showed that a direct localization model using the ellipsoid tangent sample consensus (ETSAC) performed better than other models. Dokmanic *et al.* [7] presented an RGI technique based on the properties of the Euclidean distance matrix (EDM): a matrix of inter-microphone distances. They augmented an EDM for each image source based on pairwise distances to the microphones and conducted a rank test on the augmented matrices to obtain accurate echo combinations. Lovedee-Turner and Murphy [12] proposed an RGI method to overcome the convex-shape assumption required in most previous methods. They listed candidate walls from TOA-DOA pairs and filtered out impossible candidates through post-validation processes: path validation, line-of-sight (LOS) boundary validation, and closed geometry validation. Although this method can handle non-convex room geometries, it requires the first-order reflections from every wall to be observable. Therefore, the microphone should be placed in the LOS region, where direct lines between the microphone and all the walls can be established, and the source should be relocated to multiple positions to obtain first-order reflections from every wall.

Several data-driven methods have been proposed to overcome the limitations of conventional model-based methods that rely on low-order reflections. Deep neural networks (DNN) have been used to analyze the complex relationship between low- and high-order reflections [13]–[20]. Yu and Kleijn [13] used a convolutional neural network (CNN) to analyze the relationship between the RIR and room acoustic parameters and estimated the size and absorption coefficient of shoebox rooms. Poschadel *et al.* [14] employed a convolutional recurrent neural network (CRNN) to determine the lengths, widths, and heights of shoebox rooms using simulated RIRs. Tuna *et al.* [16] also utilized a CRNN architecture to infer the 2D Cartesian coordinates of a real microphone and four imaginary microphones formed by sidewalls. This data-driven method exhibited RGI performance comparable to that of the model-based technique [21] when tested with unseen measured RIRs. Despite their outstanding RGI performance, these networks can only handle shoebox rooms because of their immutable output parameter lengths. Therefore, in our

previous studies [17], [18], we attempted to estimate various room geometries while disregarding the number of walls. This was possible by implementing an additional subnetwork that determines the confidence of the estimated wall parameters. However, the model cannot handle arbitrary geometries with curved walls because it estimates the coefficients of the plane-wall equation. To circumvent these issues, we approach the indoor geometry estimation problem as a pixel segmentation task to infer 2D floorplan and 1D height sections of arbitrarily shaped rooms.

The proposed EchoScan delivers three key contributions:

- 1) EchoScan handles more general and arbitrarily shaped rooms, including rooms with curved walls.
- 2) EchoScan adeptly interprets acoustic echoes across local and global ranges using a multi-aggregation (MA) module, which helps simultaneously infer local details and global geometries.
- 3) EchoScan fully utilizes high-order reflections, which was demonstrated through ablation studies and feature visualization analysis.

II. PROBLEM STATEMENT

Consider an indoor space or room surrounded by walls (Fig. 1), in which an audio device comprising a loudspeaker and microphone array is placed at an arbitrary position. The sound emitted from the loudspeaker is reflected by the walls and reaches the microphone array at different times. By analyzing these emitted and reflected sound waves, the acoustic fingerprint, RIR, of a room can be constructed. To secure practical accessibility for RIR measurement, this study considered an audio device that imitates an off-the-shelf voice assistant speaker with a single omnidirectional loudspeaker surrounded by microphones arranged in a circle with a fixed radius.

The indoor geometry inference problem was then formulated as a geometric pixel segmentation task using the acquired RIRs. For the i -th 3D room ($i = 1, \dots, I$), the input matrix $\mathbf{X}_i \in \mathbb{R}^{M \times N}$ of the DNN model is given by M -channel RIRs with temporal length N recorded by an audio device positioned at $\mathbf{p}_i \in \mathbb{R}^3$ in the room. The output $\mathbf{Y}_i^{3D} \in \mathbb{R}^{b \times b \times h}$

TABLE I
RGI PERFORMANCE OF PROPOSED AND ABLATION MODELS WITH DIFFERENT SPATIAL AGGREGATION FUNCTIONS

Evaluation Metric	Model	Convex							Average		
		Shoebox	Pentagonal	Hexagonal	L-LOS	L-NLOS	T-LOS	T-NLOS	Convex	Non-convex	All
IOU (%)	SP+GeM	98.33	97.64	97.44	94.99	91.55	92.79	90.12	97.80	92.36	94.69
	SP	97.84	97.21	97.10	93.18	88.39	90.87	87.70	97.38	90.04	93.18
	GeM	98.14	97.38	97.26	93.99	89.36	91.95	89.57	97.59	91.22	93.95
$MSE_{LW} (\times 10^{-3})$	SP+GeM	3.0	2.6	3.0	8.0	15.4	11.0	14.8	2.9	12.3	8.3
	SP	3.9	3.0	3.4	11.3	20.2	13.3	17.5	3.4	15.6	10.4
	GeM	3.2	2.8	3.3	10.1	20.0	12.3	15.8	3.1	14.6	9.6
$MSE_H (\times 10^{-3})$	SP+GeM	0.4	0.4	0.1	1.1	1.5	0.2	0.4	0.3	0.8	0.6
	SP	0.3	0.3	1.3	1.4	2.1	0.3	0.8	0.6	1.2	0.9
	GeM	1.7	1.3	0.7	1.1	1.5	0.7	0.6	1.2	1.0	1.1

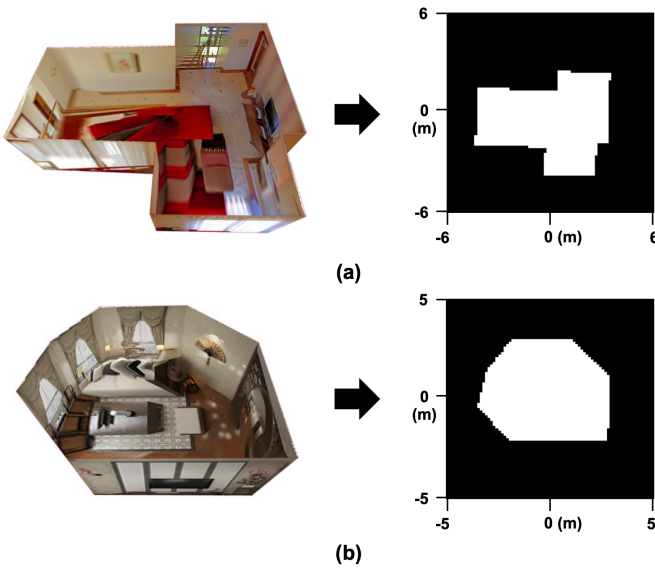


Fig. 3. Examples of real-world rooms and their floorplans. (a) Manhattan layout room containing only right-angled walls, and (b) Atlanta layout room including curved walls.

is a 3D tensor of segmented voxels defined over an arbitrarily large volume with respect to the audio device position. The output is sampled by b pixels for the length and width and h pixels for the height. Each segmented voxel contained binary values of 0 or 1, where 1 indicated the interior region of the room. By assuming that the floor and ceiling are parallel to each other and perpendicular to the sidewalls, the 3D geometry \mathbf{Y}_i^{3D} can be represented as a combination of the 2D floorplan $\mathbf{Y}_i^{LW} \in \mathbb{R}^{b \times b}$ defined in the length-width space and 1D height vector $\mathbf{y}_i^H \in \mathbb{R}^h$. Using these definitions, the model can be trained to capture hidden information from \mathbf{X}_i to infer \mathbf{Y}_i^{LW} and \mathbf{y}_i^H despite the complexity of the floorplan and heights.

III. METHODOLOGY

A. Encoder-Decoder Architecture

This study proposes an encoder-decoder architecture for estimating the indoor space geometry from RIRs, as shown in Fig. 2. The encoder extracts and compresses the spatial and temporal features \mathbf{F} from multichannel RIRs. The encoded features are aggregated into two groups of latent variables,

which are then separately fed into multi-head decoders to infer the 2D floorplan and 1D height information.

A simple encoder structure was implemented using ResNet to train the encoder so that it learns the relationships between the TOA of multichannel RIRs [22]. Furthermore, the MA module was employed to aggregate features at multiple temporal scales [23]: global and partially local. This module compresses the features of the encoded C -channel $\mathbf{F} = [\mathbf{f}_1, \dots, \mathbf{f}_C]^T \in \mathbb{R}^{C \times L}$ by using multiple global descriptors controlled by the compression parameter ρ , which is defined by Equation (1).

$$a_c(\rho) = \left(\frac{1}{\|\mathbf{f}_c\|_0} \sum_{f \in \mathbf{f}_c} f^\rho \right)^{\frac{1}{\rho}}, \text{ where } c \in \{1, \dots, C\} \quad (1)$$

where $\|\mathbf{f}_c\|_0$ represents the cardinality of vector \mathbf{f}_c . When $\rho = 1$, the function equals a sum-pooling (SP) operation and compresses the features globally. By contrast, when $\rho = \infty$, the function focuses locally as a max-pooling operation. When $\rho = 3$, the function becomes generalized mean pooling (GeM), which compresses the features to a partially local scale. The ensemble of the SP and GeM, $\mathbf{A} = [\mathbf{a}_{SP}^T, \mathbf{a}_{GeM}^T]^T = [a_1(1), \dots, a_C(1), a_1(3), \dots, a_C(3)]^T$ is exploited to capture both the local and global relations between TOAs in RIRs.

The room-geometry decoder infers the visual representation of a 3D room from the compressed latent features. A multi-head structure composed of floorplan (2D) and height (1D) decoders was designed. The floorplan decoder generated the predicted $b \times b$ -pixel image $\hat{\mathbf{Y}}_i^{LW}$ ($b = 100$), as illustrated in Fig. 3. The decoder was based on the decoder structure of the auto-encoder architecture. However, unlike the traditional auto-encoder, the proposed model incorporates skip connections that feed encoded, deep latent features into each decoder block to directly propagate indoor spatial context information to high-resolution layers. Linear projection was utilized to resolve the size mismatch between the latent features and the decoder inputs. By contrast, the height information decoder generates a $h = 40$ pixel vector $\hat{\mathbf{y}}_i^H$ through a linear layer. The inferred floorplan and height set has approximately 20 cm pixel resolution and was utilized to reconstruct the 3D room geometry.

B. Loss Function

The proposed model uses two types of loss functions for training: mean squared error (MSE) and Dice loss. The MSE

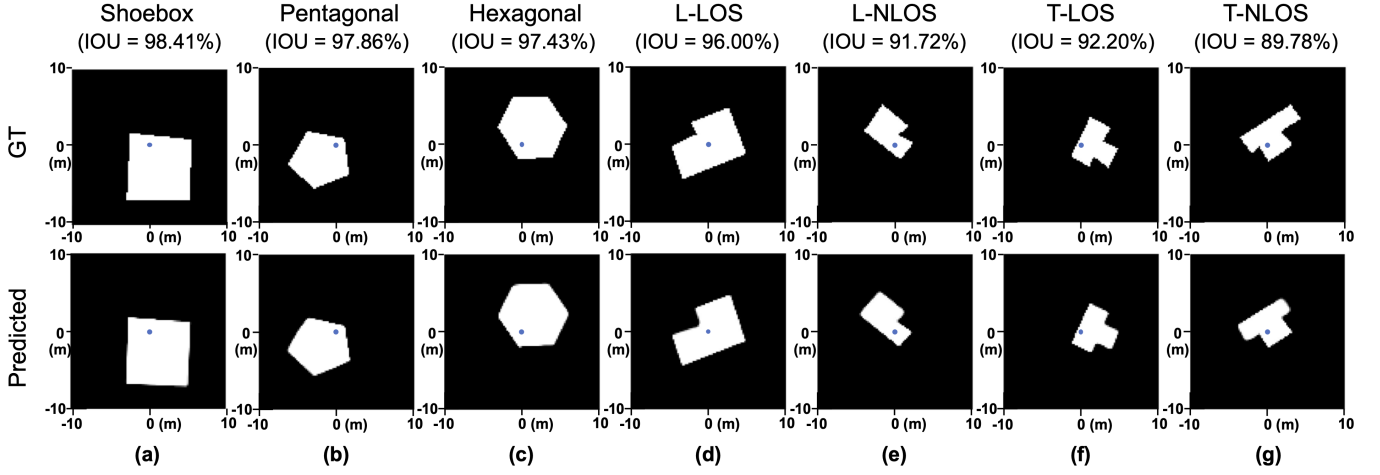


Fig. 4. Similarity in GT and the estimated floorplans. Selected examples show the average IOU performance of each standard room type. The blue dot indicates the position of the audio device.

measures the average squared difference between the predicted values and ground truth (GT) images. This guides the overall layout estimation of a given room. The Dice loss function is useful for learning specific edge details in pixel segmentation tasks and measures the alignment between the predicted and GT layouts. The Dice loss function is given by Equation (2).

$$L_{\text{Dice}}^{\text{LW}} = \frac{1}{I} \sum_{i=1}^I 1 - \frac{2\hat{\mathbf{y}}_i^{\text{LW}} \cdot \mathbf{y}_i^{\text{LW}}}{\|\hat{\mathbf{y}}_i^{\text{LW}} + \mathbf{y}_i^{\text{LW}}\|_1}, \quad (2)$$

where \mathbf{y}^{LW} is the vectorized form of the matrix \mathbf{Y}^{LW} , the (\cdot) operator indicates the dot product of the vectors, and $\|\cdot\|_1$ is the 1-norm of a vector. The total loss function is given by the weighted sum of the MSE loss for the floorplan, MSE loss for the height, and Dice loss, as expressed in Equation (3).

$$L_{\text{total}} = L_{\text{MSE}}^{\text{LW}} + \alpha L_{\text{Dice}}^{\text{LW}} + \beta L_{\text{MSE}}^{\text{H}} \quad (3)$$

The weights $\alpha = 0.3$ and $\beta = 1$ were heuristically determined and showed good performance in all experiments.

The circular microphone array used in this study does not distinguish ceiling reflections from floor reflections. To address this, we employed the permutation invariant training (PIT) technique [24]. It compares the estimated height vector with the original and flipped GT height vectors and updates the network with one that gives the lowest loss. After the inference is completed, the shorter side of the image center is considered the floor, because audio devices are usually positioned closer to the floor than to the ceiling.

IV. EXPERIMENT SETUP

A. Data Preparation

Large RIR datasets of simple-shaped rooms (standard room dataset) and complex-shaped rooms (real-world room dataset) were created to extensively analyze and validate the proposed model. The following sections describe the RIR dataset construction.

1) *Standard Room Dataset*: The standard room dataset included RIRs simulated from five types of simple-shaped rooms: shoebox, pentagonal, hexagonal, L-type, and T-type. The dataset comprises 600k RIRs for training and 1k RIRs for testing. Despite their simple shapes, all RIRs in this dataset were simulated in non-identical room configurations. The room sizes were randomly populated, and an additional crumpling step was introduced to diversify the aspect ratios. The rooms used for the test data belonged to one of the five types; however, their shapes differ from those of the rooms used for the training dataset.

Initially, the room type was chosen randomly from the five types, and the room size parameters $\mathbf{s} = [s_l, s_w, s_h]$ denoting length, width, and height, were then populated randomly from uniform distributions within the ranges $[2, 5]$, $[2, 5]$, and $[3, 5]$ m, respectively. A prototype room was then generated from the size parameter \mathbf{s} and the corresponding vertex matrix $\mathbf{V} = [\mathbf{v}_1, \dots, \mathbf{v}_K]^T \in \mathbb{R}^{K \times 2}$, which represents a 2D K -sided floorplan. The vertex matrix for the shoebox rooms was defined as $\mathbf{V}^{(S)} = [(-s_l, -s_w), (-s_l, s_w), (s_l, s_w), (s_l, -s_w)]$. For the pentagonal and hexagonal rooms, each vertex position \mathbf{v}_k was set to $\mathbf{v}_k = [s_l \cos(2\pi k/K), s_w \cos(2\pi k/K)]^T$. For an L-type room, a shoebox room with lengths s_l and s_w was generated first, and then the cutout positions $[\mu_l, \mu_w]^T$ were randomly determined within the ranges $[0, 0.5s_l]$ and $[0, 0.5s_w]$, respectively. Similarly, for a T-type room, $\mu_l^{(1)}$, $\mu_l^{(2)}$, and μ_w were populated randomly within the ranges $[-0.75s_l, -0.25s_l]$, $[0.25s_l, 0.75s_l]$, and $[-0.5s_w, 0]$ respectively.

The room shapes were then crumpled and rotated by randomly shifting the generated vertices by up to 0.5 m and rotating within $[0, 2\pi]$ in the length-width space. The crumpling and rotation enabled the model to adapt to a wide range of real-world room shapes. A GT 2D floor plan image was then generated by positioning a cross-sectional image of the generated room shape inside an image template of $b \times b$ pixels. The positioning was such that the audio device in the room was always at the center of the image template (Fig. 4).

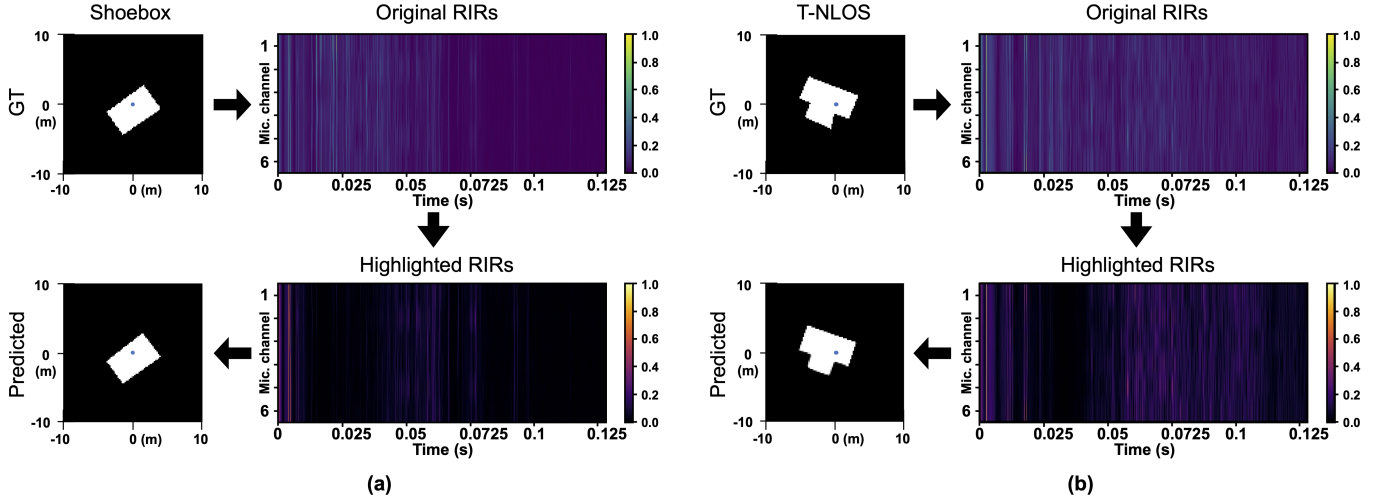


Fig. 5. Visualization of temporal activation using Grad-CAM. (a) and (b) display the Grad-CAM results for the shoebox and T-NLOS rooms, respectively. The highlighted areas actively change based on the characteristics of each room. The audio device is denoted by a blue dot.

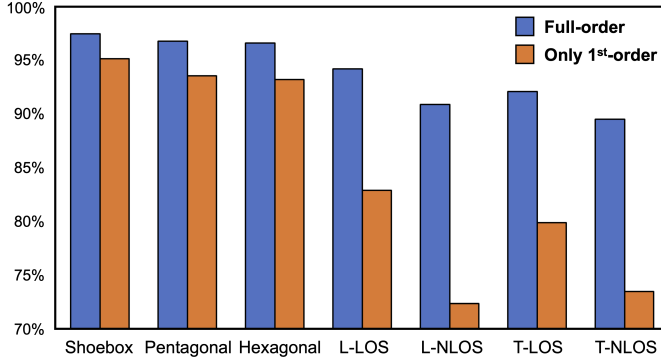


Fig. 6. Quantitative performance (3D IOU) comparison between RIRs with full-order and only first-order reflections. The RGI performance significantly decreases when estimating L- and T-type rooms using RIRs that contain only first-order reflections. This indirectly suggests that EchoScan utilizes high-order reflections.

The audio device was configured using a circular microphone array of six omnidirectional microphones arranged on a ring with a loudspeaker placed at its center and a 5 cm radius. The device was then randomly placed within 70% of the length-width space of the room and a height range of [1, 1.5] m from the floor. The random positioning of the device is equivalent to a translated effect on the room configuration. Depending on the position of the audio device, the walls can be in either LOS or non-line-of-sight (NLOS) conditions. When straight-line connections can be made from the audio device to all walls without other walls obstructing, the room satisfies the LOS condition.

2) *Real-world Room Dataset*: To validate the performance of the proposed model on more realistic room geometries, we employed a publicly available room dataset constructed from the layouts of real-world rooms. The dataset included two types of layouts popularly utilized in vision-based approaches: the Manhattan layout [25] and the Atlanta layout [26]. In both layouts, the sidewalls were vertical to the horizontal floors

and ceilings. However, the Manhattan layout has sidewalls that strictly meet at right angles, whereas the Atlanta layout does not, allowing for more flexible room shapes. The real-world room dataset used in this work comprises 1,249 layouts, including 1,127 Manhattan layouts from PanoContext [27] and Stanford2D3D [28], as well as 122 Atlanta layouts from Matterport3D [29] and Structured3D [30]. The data setup followed that of HorizonNet [31] and AtlantaNet [26].

The real-world measured dataset was divided into fine-tuning and test sets using an 8:2 ratio to obtain 1k and 249 layouts, respectively. The model, initially trained on a standard room dataset, was subsequently fine-tuned using the fine-tuning dataset with 1k data was augmented to 100k rooms through various steps: size augmentation using scaling factors randomly chosen between 0.5 to 2, rotation, and translation augmentation, as described in Section IV-A1. A test dataset with 249 layouts was used to assess the generalization performance of the model. It was separated into ‘Seen’ and ‘Unseen’ datasets. The ‘Seen’ dataset includes the room types from the fine-tuning dataset that have different room sizes, rotations, and translations. The ‘Unseen’ dataset consists of distinctive room shapes intentionally excluded from the fine-tuning dataset.

3) *RIR Simulation*: The raytracing engine of the Pyroomacoustics software [32] was employed to generate multichannel RIRs for general polyhedral rooms. Because the loudspeakers and microphones maintained consistent distances, the direct parts of the RIRs were omitted. RIRs were generated at an 8 kHz sampling rate and included $N = 1024$ samples in the time dimension. With this configuration, a single sample represents approximately 4.3 cm of sound travel, and the total length of an RIR corresponds to 44 m. Gaussian noise was added to emulate standard noise disturbances. The background noise was adjusted to ensure a signal-to-noise ratio (SNR) between [10, 20] dB relative to the overall energy of the RIR.

Wall absorption greatly affects the strength and dispersion of echoes. A set of typical absorption materials for floors, ceil-

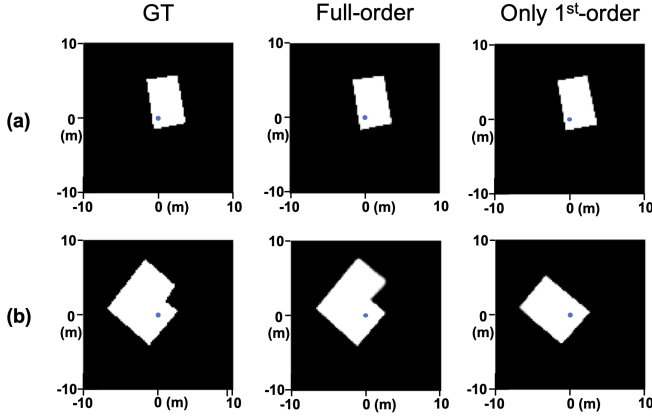


Fig. 7. Comparison of indoor geometry estimation performance between RIRs with full-order and only first-order reflections. (a) Shoebox room and (b) L-NLOS room. The L-type room is estimated as a shoebox room when the RIRs are truncated to include only first-order reflections.

ings, and sidewalls defined in [32] were utilized and randomly assigned to each room. These materials include linoleum on concrete, carpet, and audience floor (wooden floor) for floors; gypsum boards, metal panels, and plasterboards for ceilings; and hard surfaces, rough concrete, rough lime washes, glass windows, and plasterboards for sidewalls.

B. Training Configuration

Four NVIDIA GeForce RTX 2080Ti GPUs with batch sizes of 32 were employed to train the model. The learning rate was varied using the cosine-annealing warmup restart scheduler [33] with an initial learning rate of $1e^{-2}$ to a minimum of $1e^{-6}$. The Adam optimizer [34] was used for backpropagation. During training, variable-length time masking was applied to the input RIRs [35] to enhance the robustness of the model. Three masks were applied to random temporal locations of RIRs, and the lengths of the masks were randomly chosen within [0, 100] samples.

C. Evaluation Metrics

The performance of the proposed model was verified using two performance evaluation metrics. First, MSE was used to evaluate both floorplan and height values. Second, the intersection over union (IOU) was adopted as a similarity measure at the pixel or voxel level. The IOU for the room geometry is defined by Equation (4).

$$\text{IOU} = \frac{1}{I} \sum_{i=1}^I \frac{\hat{\mathbf{y}}_i^{3D} \cdot \mathbf{y}_i^{3D}}{\|\hat{\mathbf{y}}_i^{3D} + \mathbf{y}_i^{3D}\|_1 - \hat{\mathbf{y}}_i^{3D} \cdot \mathbf{y}_i^{3D}}, \quad (4)$$

where \mathbf{y}^{3D} is the vectorized form of the matrix \mathbf{Y}^{3D} .

V. EXPERIMENTAL RESULTS

A. Ablation Studies on the MA Module

To demonstrate the effectiveness of the proposed model and its MA modules, we conducted ablation studies with different combinations of aggregation functions: MA modules with SP,

TABLE II
PERFORMANCE COMPARISON (3D IOU, %) OF PROPOSED AND VISION-BASED METHODS ON REAL-WORLD ROOM DATASET

Room type (# of corners)	DulaNet [36]	HorizonNet [31]	AtlantaNet [26]	Ours (Unseen)	Ours (Seen)
Manhattan (4)	77.0	81.9	82.6	93.3	94.5
Manhattan (6)	78.8	82.3	80.1	87.9	89.1
Manhattan (8)	71.0	71.8	71.2	90.1	91.2
Atlanta (5–6)	–	74.5	84.3	81.7	85.2
Atlanta (7–8)	–	65.0	78.4	95.4	96.0
Atlanta (>8)	–	64.4	75.3	87.4	89.2

GeM, and SP and GeM. The comparison results in Table I show that using the GeM function alone outperformed the SP function alone in terms of IOU and MSE scores, and the MA model with both performed the best in all room types. The performance differences between the MA and single-aggregation modules are clear in complex rooms such as L- and T-type rooms. This indicates that, although prioritizing a partially local relationship within RIRs (GeM) is considered more crucial than broad-range attention (SP), both information types are vital.

B. RGI Performance of EchoScan

The performance of the proposed model in estimating 3D indoor space geometry is presented in Fig. 4 and Table I. The overall result shows over 90% IOU for all standard room types and a negligible MSE for height estimation. This indicates that the height estimation task is sufficiently simple to be accomplished using a decoder with a single linear layer. The first-order reflections present distinct peaks in RIRs; therefore, encoding features related to first-order reflections requires minimal effort. Thus, the shoebox rooms showed the best performance for both MSE (LW) and IOU, although it tended to decrease in non-convex room shapes, for which some first-order reflections were missing in the measured RIRs. In addition, the performances in LOS and NLOS cases of L- and T-type rooms were notably different, even for rooms of the same type.

To illustrate the geometric similarity between the GT and the estimated rooms, we selected rooms whose performances were similar to the mean IOUs in Table I and depicted them in Fig. 4. For the convex rooms illustrated in Figs. 4(a)–(c), the model could accurately predict the room shapes. For the non-convex LOS rooms shown in Figs. 4(d)–(g), although the estimations were less accurate than those for convex rooms, the accuracy was still high. Particularly, for the non-convex NLOS rooms shown in Figs. 4(e) and (g), rooms were underestimated because some walls are invisible from the device position. However, the overall shapes, including invisible walls, can remarkably still be estimated, which was not possible using vision- or previous sound-based approaches. These results highlight the significance of utilizing high-order reflection information based on sound propagation characteristics to predict NLOS-type rooms.

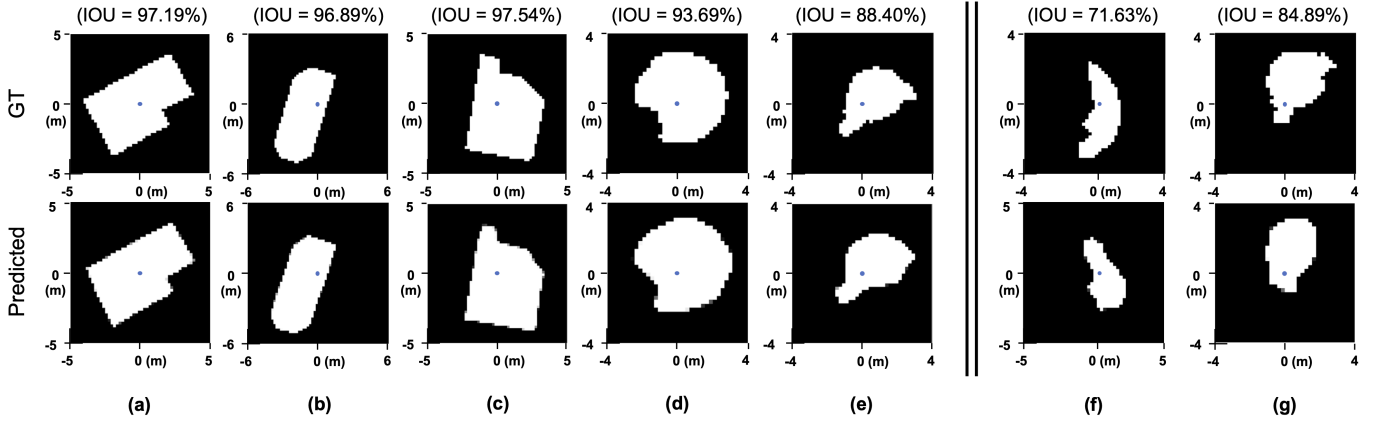


Fig. 8. Selected floorplan images showing the average IOU performance on the real-world room dataset. (a) Manhattan layout with 6 corners, (b)–(c) Atlanta layout with 7–8 corners, (d)–(e) Atlanta layout with over 8 corners, and (f)–(g) bad RGI examples of the Atlanta layout with over 8 corners

C. Role of High-Order Reflections

To assess whether our model considers higher-order reflections, we conducted two distinct investigations: model interpretation and data analysis. For the model interpretation, gradient-weighted class activation mapping (Grad-CAM) [37] was utilized to highlight the temporal areas in the input RIRs that affect the predictions of the model. As depicted in Fig. 5(a), for a simple shoebox room satisfying the LOS condition, most activations occurred early in the temporal region, emphasizing first-order reflections. This result is similar to that of conventional sound-based approaches that exploit early visible reflections. Conversely, for more complex rooms, such as a T-type room with NLOS walls, as the one shown in Fig. 5(b), activation is suppressed in the early temporal region (approximately 0.01 s) but also highlights high-order reflections spanning from 0.05 to 0.1 s. These highlighted segments correspond to sound travel distances of approximately 17 to 34 m, which signifies that the model actively utilized late echoes to determine complex room shapes.

To further confirm the utilization of high-order reflections, we compared the performance of two distinct EchoScan models trained using RIRs with full- and first-order reflections. The results are shown in Figs. 6 and 7, which reveal a notable disparity. When the model was constrained to first-order reflections, its IOU score for non-convex rooms decreased considerably, particularly in NLOS scenarios, compared to the model trained with full-order reflections. Specifically, the model trained with limited reflections could accurately estimate a shoebox room, as shown in Fig. 7(a), it struggles with more complex geometries such as a non-convex L-NLOS room (Fig. 7(b)), which often oversimplifies a room into a basic shoebox shape. This result also indicates that EchoScan uses high-order reflections to infer complex room geometries.

D. Performance Analysis for Real-world Measured Arbitrary Rooms

The proposed model was compared with vision-based methods [26], [31], [36] using the real-world room dataset. Table II presents the results. AtlantaNet demonstrated superior

performance, particularly for Atlanta rooms, while maintaining results comparable to those of HorizonNet in the Manhattan configuration. Remarkably, the proposed EchoScan outperformed all vision-based techniques in most types of rooms. Compared with AtlantaNet, Manhattan with 8 corners and Atlanta with 7–8 corners showed the greatest developments, with IOU scores increasing by 18.9% and 17.0%, respectively. Exceptionally, the decrease in performance in the Atlanta layout with 5–6 corners was attributable to the many invisible walls of the L-shaped rooms in the dataset. Nevertheless, their differences from vision-based methods were subtle. Additionally, the performance gap between the ‘Seen’ and ‘Unseen’ datasets typically ranged around only 1 to 2%, which indicates the robustness of EchoScan when working with unseen shapes.

Fig. 8 compares the GT floorplans and RGI results for the selected rooms from the real-world room dataset. Notably, Figs. 8(a)–(e) show that EchoScan provides acceptable RGI results for various room shapes. For the Manhattan room with 6 corners (Fig. 8(a)) and the long Atlanta room with 8 corners (Fig. 8(b)), EchoScan accurately predicted with a high IOU score of approximately 97%. Even in a room in Atlanta with 7 corners (Fig. 8(c)), which includes an invisible wall, EchoScan achieved an impressive IOU score of approximately 98%. Figs. 8(d)–(e) demonstrate that EchoScan can infer complex Atlanta rooms with curved walls and numerous corners. Notably, in Fig. 8(e), the difference between the GT and estimation only occurs in a small region on the right-hand side. Finally, some poorly estimated cases were selected as depicted in Figs. 8(f)–(g). In these cases, EchoScan failed to accurately predict the room shape, providing low IOU scores of approximately 71% and 84%. However, EchoScan roughly approximated the position, size, and orientation of the room. In summary, EchoScan shows remarkable geometry estimation performance across the Manhattan and Atlanta layouts, which include walls whose first-order reflections are unmeasurable at the device position and curved walls that are undetectable using conventional sound-based techniques.

VI. CONCLUSION

As real-world rooms exhibit complex and irregular shapes including curved walls and those producing echoes, which are undetectable from the position of the device, RGI has become a challenging problem that cannot be addressed using parameter estimation methods. To address this problem, a more general framework that can comprehensively analyze high-order reflections must be developed. Thus, this study proposed a sound-based framework called EchoScan for inferring the geometry of rooms with complex shapes. To this end, first, we designed EchoScan as a pixel-segmentation network that estimates segmented floorplan images and room-height vectors. Subsequently, an MA module that merges the latent features extracted from the ResNet-based encoder at different temporal scales was introduced to facilitate the use of higher-order reflections. We validated the RGI performance of EchoScan and its capability to capture high-order reflections accurately using a standard room dataset. Furthermore, its robustness and generalization ability were assessed in practical situations using real-world datasets. EchoScan performed remarkably on these diverse room layouts, demonstrating its potential as a promising alternative to vision-based methods, specifically in environments that lack visual clues.

REFERENCES

- [1] M. Liu, S. Fang, H. Dong, and C. Xu, "Review of digital twin about concepts, technologies, and industrial applications," *J. Manuf. Syst.*, vol. 58, pp. 346–361, 2021.
- [2] V. Valimaki, J. D. Parker, L. Savioja, J. O. Smith, and J. S. Abel, "Fifty years of artificial reverberation," *IEEE Trans. Audio, Speech, Language Process.*, vol. 20, no. 5, pp. 1421–1448, 2012.
- [3] F. Antonacci, J. Filos, M. R. Thomas, E. A. Habets, A. Sarti, P. A. Naylor, and S. Tubaro, "Inference of room geometry from acoustic impulse responses," *IEEE Trans. Audio, Speech, Language Process.*, vol. 20, no. 10, pp. 2683–2695, 2012.
- [4] L. Remaggi, P. J. Jackson, W. Wang, and J. A. Chambers, "A 3d model for room boundary estimation," in *Proc. IEEE Int. Conf. Acoust., Speech, Signal Process.*, South Brisbane, QL, Australia, 2015, pp. 514–518.
- [5] H. Naseri and V. Koivunen, "Indoor mapping based on time delay estimation in wireless networks," in *Proc. IEEE Int. Conf. Acoust., Speech, Signal Process.*, South Brisbane, QL, Australia, 2015, pp. 2424–2428.
- [6] I. Dokmanić, Y. M. Lu, and M. Vetterli, "Can one hear the shape of a room: The 2-d polygonal case," in *Proc. IEEE Int. Conf. Acoust., Speech, Signal Process.*, Prague, Czech Republic, 2011, pp. 321–324.
- [7] I. Dokmanić, R. Parhizkar, A. Walther, Y. M. Lu, and M. Vetterli, "Acoustic echoes reveal room shape," *Proc. Natl. Acad. Sci. U.S.A.*, vol. 110, no. 30, pp. 12 186–12 191, 2013.
- [8] Y. El Baba, A. Walther, and E. A. Habets, "3d room geometry inference based on room impulse response stacks," *IEEE/ACM Trans. Audio, Speech, Language Process.*, vol. 26, no. 5, pp. 857–872, 2017.
- [9] L. Remaggi, P. J. Jackson, P. Coleman, and W. Wang, "Acoustic reflector localization: Novel image source reversion and direct localization methods," *IEEE/ACM Trans. Audio, Speech, Language Process.*, vol. 25, no. 2, pp. 296–309, 2016.
- [10] T. Rajapaksha, X. Qiu, E. Cheng, and I. Burnett, "Geometrical room geometry estimation from room impulse responses," in *Proc. IEEE Int. Conf. Acoust., Speech, Signal Process.*, Shanghai, China, 2016, pp. 331–335.
- [11] S. Park and J.-W. Choi, "Iterative echo labeling algorithm with convex hull expansion for room geometry estimation," *IEEE/ACM Trans. Audio, Speech, Language Process.*, vol. 29, pp. 1463–1478, 2021.
- [12] M. Lovedee-Turner and D. Murphy, "Three-dimensional reflector localisation and room geometry estimation using a spherical microphone array," *J. Acoust. Soc. Am.*, vol. 146, no. 5, pp. 3339–3352, 2019.
- [13] W. Yu and W. B. Kleijn, "Room acoustical parameter estimation from room impulse responses using deep neural networks," *IEEE/ACM Trans. Audio, Speech, Language Process.*, vol. 29, pp. 436–447, 2020.
- [14] N. Poschadel, R. Hupke, S. Preihs, and J. Peissig, "Room geometry estimation from higher-order ambisonics signals using convolutional recurrent neural networks," in *Proc. Audio Eng. Soc. Convention 150*, Virtual, 2021.
- [15] S. Gao, X. Wu, and T. Qu, "Room geometry blind inference based on the localization of real sound source and first order reflections," *arXiv preprint arXiv:2207.10478*, 2022.
- [16] C. Tuna, A. Akat, H. N. Bicer, A. Walther, and E. A. Habets, "Data-driven 3d room geometry inference with a linear loudspeaker array and a single microphone," in *Proc. Eur. Acoust. Assoc. (Forum Acousticum 2023)*, Torino, Italy, 2023.
- [17] I. Yeon and J.-W. Choi, "3d room geometry inference from multichannel room impulse response using deep neural network," in *Proc. 24th Int. Congr. Acoust.*, Gyeongju, Korea, 2022.
- [18] I. Yeon and J.-W. Choi, "Rgi-net: 3d room geometry inference from room impulse responses in the absence of first-order echoes," *arXiv preprint arXiv:2309.01513*, 2023.
- [19] A. Luo, Y. Du, M. Tarr, J. Tenenbaum, A. Torralba, and C. Gan, "Learning neural acoustic fields," *Adv. Neural Inf. Process. Syst.*, vol. 35, pp. 3165–3177, 2022.
- [20] S. Purushwalkam, S. V. A. Gari, V. K. Ithapu, C. Schissler, P. Robinson, A. Gupta, and K. Grauman, "Audio-visual floorplan reconstruction," in *Proc. IEEE Int. Conf. Comput. Vis.*, Virtual, 2021, pp. 1183–1192.
- [21] C. Tuna, A. Canclini, F. Borra, P. Götz, F. Antonacci, A. Walther, A. Sarti, and E. A. Habets, "3d room geometry inference using a linear loudspeaker array and a single microphone," *IEEE/ACM Trans. Audio, Speech, Language Process.*, vol. 28, pp. 1729–1744, 2020.
- [22] K. He, X. Zhang, S. Ren, and J. Sun, "Deep residual learning for image recognition," in *Proc. IEEE Comput. Soc. Conf. Comput. Vis. Pattern Recognit.*, Las Vegas, NV, USA, 2016, pp. 770–778.
- [23] H. Jun, B. Ko, Y. Kim, I. Kim, and J. Kim, "Combination of multiple global descriptors for image retrieval," *arXiv preprint arXiv:1903.10663*, 2019.
- [24] D. Yu, M. Kolbæk, Z.-H. Tan, and J. Jensen, "Permutation invariant training of deep models for speaker-independent multi-talker speech separation," in *Proc. IEEE Int. Conf. Acoust., Speech, Signal Process.*, New Orleans, LA, USA, 2017, pp. 241–245.
- [25] J. M. Coughlan and A. L. Yuille, "Manhattan world: Orientation and outlier detection by bayesian inference," *Neural Computation*, vol. 15, no. 5, pp. 1063–1088, 2003.
- [26] G. Pintore, M. Agus, and E. Gobbetti, "Atlantnet: inferring the 3d indoor layout from a single 360° image beyond the manhattan world assumption," in *Proc. Eur. Conf. Comput. Vis.* Glasgow, UK: Springer, 2020, pp. 432–448.
- [27] Y. Zhang, S. Song, P. Tan, and J. Xiao, "Panocontext: A whole-room 3d context model for panoramic scene understanding," in *Proc. Eur. Conf. Comput. Vis.* Zurich, Switzerland: Springer, 2014, pp. 668–686.
- [28] I. Armeni, S. Sax, A. R. Zamir, and S. Savarese, "Joint 2d-3d-semantic data for indoor scene understanding," *arXiv preprint arXiv:1702.01105*, 2017.
- [29] A. Chang, A. Dai, T. Funkhouser, M. Halber, M. Niessner, M. Savva, S. Song, A. Zeng, and Y. Zhang, "Matterport3d: Learning from rgb-d data in indoor environments," *Int. Conf. 3D Vis.*, 2017.
- [30] J. Zheng, J. Zhang, J. Li, R. Tang, S. Gao, and Z. Zhou, "Structured3d: A large photo-realistic dataset for structured 3d modeling," in *Proc. Eur. Conf. Comput. Vis.* Glasgow, UK: Springer, 2020, pp. 519–535.
- [31] C. Sun, C.-W. Hsiao, M. Sun, and H.-T. Chen, "Horizonnet: Learning room layout with 1d representation and pano stretch data augmentation," in *Proc. IEEE Comput. Soc. Conf. Comput. Vis. Pattern Recognit.*, Long Beach, CA, USA, 2019, pp. 1047–1056.
- [32] R. Scheibler, E. Bezzam, and I. Dokmanić, "Pyroomacoustics: A python package for audio room simulation and array processing algorithms," in *Proc. IEEE Int. Conf. Acoust., Speech, Signal Process.* Calgary, AB, Canada: IEEE, 2018, pp. 351–355.
- [33] I. Loshchilov and F. Hutter, "Sgdr: Stochastic gradient descent with warm restarts," in *Proc. Int. Conf. Learn. Repr.*, Toulon, France, 2017.
- [34] D. P. Kingma and J. Ba, "Adam: A method for stochastic optimization," in *Proc. Int. Conf. Learn. Repr.*, San Diego, CA, USA, 2015.
- [35] D. S. Park, W. Chan, Y. Zhang, C.-C. Chiu, B. Zoph, E. D. Cubuk, and Q. V. Le, "SpecAugment: A simple data augmentation method for automatic speech recognition," in *Proc. Conf. Int. Speech Comm. Assoc. (INTERSPEECH)*. Graz, Austria: ISCA, 2019.
- [36] S.-T. Yang, F.-E. Wang, C.-H. Peng, P. Wonka, M. Sun, and H.-K. Chu, "Dula-net: A dual-projection network for estimating room layouts from a single rgb panorama," in *Proc. IEEE Comput. Soc. Conf. Comput. Vis. Pattern Recognit.*, Long Beach, CA, USA, 2019, pp. 3363–3372.

- [37] R. R. Selvaraju, M. Cogswell, A. Das, R. Vedantam, D. Parikh, and D. Batra, “Grad-cam: Visual explanations from deep networks via gradient-based localization,” in *Proc. IEEE Int. Conf. Comput. Vis.*, Venice, Italy, 2017, pp. 618–626.



Immo Yeon (Student Member, IEEE) received an A.A. degree in audio production from the Dong-ah Institute of Media and Arts (DIMA), South Korea in 2018; a B.S. degree in audio engineering from the National Institute for Lifelong Education (NILE), South Korea in 2019; and an M.S. degree in electrical engineering from Hanyang University, South Korea in 2021. He is currently pursuing a Ph.D. degree at the School of Electrical Engineering of the Korea Advanced Institute of Science and Technology (KAIST), South Korea. His research

interests include signal processing, room acoustics, spatial audio, and deep learning.



Iljoo Jeong received a B.S. degree in mechanical engineering from Ajou University, Suwon, South Korea in 2016. He is currently a Ph.D. candidate in the Department of Mechanical Engineering at Pohang University of Science and Technology (POSTECH), South Korea. He is currently a guest researcher at the Korea Research Institute of Standards and Science (KRISS), Daejeon, South Korea. His research interests include deep learning, smart manufacturing, acoustics, and inverse problem-solving.



Seungchul Lee received a B.S. degree in mechanical and aerospace engineering from Seoul National University, Seoul, South Korea in 2001, and M.S. and Ph.D. degrees in mechanical engineering from the University of Michigan, Ann Arbor, MI, USA in 2008 and 2010, respectively. He is currently an Associate Professor at the Department of Mechanical Engineering of the Korea Advanced Institute of Science and Technology (KAIST), Daejeon, South Korea. His research focuses on industrial artificial intelligence for mechanical systems, smart manufacturing, materials, and healthcare. His research extends to both knowledge-

guided AI and AI-driven knowledge discovery.



Jung-Woo Choi (Member, IEEE) received the B.Sc., M.Sc., and Ph.D. degrees in mechanical engineering from the Korea Advanced Institute of Science and Technology (KAIST), South Korea in 1999, 2001, and 2005, respectively. From 2006 to 2007, he was a postdoctoral researcher at the Institute of Sound and Vibration Research of the University of Southampton, Southampton, U.K. From 2007 to 2011, he worked with Samsung Electronics at the Samsung Advanced Institute of Technology, Suwon, South Korea. He was a Research Associate

Professor in the Department of Mechanical Engineering at KAIST until 2014. In 2015, he joined the School of Electrical Engineering of the KAIST as an Assistant Professor. In 2018, he became an Associate Professor. His current research interests include sound-field reproduction, sound focusing, array signal processing, and their applications. He is a member of the Acoustical Society of America at the Institute of Noise Control Engineers, USA, and the Korean Society of Noise and Vibration Engineering.